Photoionization of neutral iron from the ground and excited states

O. Zatsarinny[*] and K. Bartschat

Drake University, Des Moines, Iowa 50311, USA

L. Fernandez-Menchero

The Queen's University of Belfast, Belfast BT7 1NN, United Kingdom

S. S. Tayal

Clark Atlanta University, Atlanta, Georgia 30314, USA

The B-spline R-matrix method is used to investigate the photoionization of neutral iron from the ground and excited states in the energy region from the ionization thresholds to 2 Ry. The multiconfiguration Hartree-Fock method in connection with adjustable configuration expansions and term-dependent orbitals is employed for an accurate representation of the initial states of Fe I and the target wave functions of Fe II. The close-coupling expansion contains 261 LS states of Fe II and includes all levels of the $3d^6 4s$, $3d^5 4s^2$, $3d^7$, $3d^6 4p$, and $3d^5 4s 4p$ configurations. Full inclusion of all terms from the principal configurations considerably changes both the low-energy resonance structure and the energy dependence of the background cross sections. Partial cross sections are analyzed in detail to clarify the most important scattering channels. Comparison with other calculations is used to place uncertainty bounds on our final photoionization cross sections and to assess the likely uncertainties in the existing data sets.

I. INTRODUCTION

The enormous importance of iron-peak elements for astronomical observations is well known. Neutral Fe and its ions play important roles in many aspects of astrophysics. Due to its large opacity contribution, Fe has come to serve as a fundamental reference point for many chemical analyses and their interpretations [1]. The analysis and diagnostics of a broad range of stellar and nebular spectra require accurate radiative and collision atomic data. Accurate photoionization cross sections for neutral iron are a requirement for accurate chemical abundances in late-type stars [2]. The cross sections for partial processes from both ground and low-lying excited states are usually a minimum requirement for detailed non-local thermodynamic equilibrium modeling. Because of the importance of these atomic data and the complete lack of experiments, major theoretical and computational efforts have been devoted to this system over the past decades. Presently, however, both electron-impact excitation rates and photoionization cross sections for Fe still represent a significant source of uncertainty in the models [3].

Over several decades, calculations of photoionization cross sections for Fe I were carried out in a variety of approximations with increasing size and sophistication. An early photoionization calculation was reported by Kelly and Ron [4,5] using a many-body perturbation method. Reilman and Manson [6] and Verner *et al.* [7] employed central-field approximations. These calculations ignored important coupling effects and resonances, which in turn led to an underestimation of the photoionization cross sections. The earliest R-matrix calculation for neutral iron was reported by Baluja *et al.* [8]. They considered photoionization from the ground state and included in their approximation only the four lowest states of the Fe II residual ion. More extensive calculations were carried out by Sawey and Berrington [9], who used an expansion for Fe II including $3d^7$, $3d^6(^5 D)4s$, $3d^6(^5 D)4p$, and $3d^5(^6 S)4s^2$ configurations. Due to computational limitations, these earliest R-matrix calculations also clearly missed essential coupling effects and neglected resonance series converging to higher-lying thresholds. Much more extensive R-matrix calculations were reported by Bautista [10], who included 15 configurations and the lowest 52 LS terms of Fe II. Significant corrections, both for the background cross sections and the resonance structure, were obtained in comparison to the previous results.

The cross sections of Bautista [10] were adopted in many stellar atmosphere modeling codes and used in numerous applications. Given the significance of photoionization and electron-impact excitation data for neutral iron in cool-stars research and the advances in computational resources over the past two decades, Bautista *et al.* [3] decided to revisit the problem of Fe photoionization and provide data of improved accuracy. Their new R-matrix photoionization calculations included 35 configurations and 134 LS close-coupling terms of the target ion. The accuracy of the target states, however, was not discussed. Comparison with the previous results in the 52-state approximation showed further considerable corrections to the total and partial cross sections.

---
[*]oleg.zatsarinny@drake.edu

The above discussion shows that, despite the large computational efforts devoted in the past, one still cannot state that convergence of the predicted photoionization cross sections for neutral iron has been achieved to date. The purpose of the present work, therefore, is to perform even more elaborate and extensive calculations for photoionization of Fe I than what is currently available. The further improvements include both principal aspects of the collision calculations, namely, the accuracy of the target states and the size of the close-coupling expansion.

The calculations of scattering processes on iron and its first ions is a very challenging computational problem. The accurate representation of the open $3d$ subshell target states requires extensive configuration-interaction (CI) expansions, whereas the very large number of energy levels and transitions involved in the spectrum requires large close-coupling (CC) expansions. As an additional complication, we note that the individual orbitals in the $3d^x4s^2$, $3d^{x+1}4s$, and $3d^{x+2}$, and other target configurations are very term-dependent. This makes it extremely difficult to achieve a sufficiently accurate target description with standard CI procedures. Hence, computer codes that require a set of orthogonal one-electron orbitals, such as RMATRX I [11] and RMATRX II [12], can only account for such term dependence by large CI expansions that involve a number of specially designed pseudo-orbitals. In this case, one needs to carefully consider the balance of the N-electron target structure and the $(N+1)$-electron collision problems. This represents a serious challenge even for experienced users of these codes.

The present calculations were carried out with the *B*-spline *R*-matrix (BSR) code [13], where a *B*-spline basis is employed to represent the one-electron orbitals. Within this method, nonorthogonal sets of term-dependent orbitals are extensively used in both the target description and the representation of the scattering functions. That, in connection with multiconfiguration target expansions, provides a systematic way to account for a variety of correlation and relaxation effects. This feature was illustrated in detail in our recent calculations for electron collisions with Fe I [14] and Fe II [15], where the flexibility of the code allowed us to generate a target description of unprecedented accuracy for collision calculations. At the same time, abolishing the orthogonality constraints imposed on the scattering orbitals in the BSR code ensures a numerically consistent treatment of the N-electron target and the $(N+1)$-electron collision problems. This is very important for an accurate description of the near-threshold resonance structure.

The present close-coupling expansion contains *all* terms of the $3d^64s$, $3d^54s^2$, $3d^7$, $3d^64p$, and $3d^54s4p$ configurations of Fe I. This set of final target states covers all major channels for the photoionization of neutral iron and thus provides a basis for approaching convergence for the predicted photoionization cross sections. As illustrated below, including all terms from the $3d^64p$ and $3d^54s4p$ configurations considerably changes the calculated low-energy resonance structure and energy dependence for photoionization of excited states of Fe. The present calculations can thus help in assessing the accuracy of the existing data sets and in estimating their uncertainties.

II. COMPUTATIONAL METHODS

A. Structure calculations

The photoionization calculations require a consistent representation of both the initial states of Fe I and the final states of Fe II. Modeling of atomic structure, however, is a difficult task due to the presence of the open $3d$ subshell. The near degeneracy of the $3d^x$, $3d^{x-1}4s$, $3d^{x-2}4s^2$, and other configurations for the neutral elements and their lowly charged ions results in very complex spectra that are strongly influenced by configuration interaction. Therefore the calculations become extremely cumbersome, and the spectra exhibit a very complex structure that is difficult to analyze. Accounting appropriately for correlation effects requires one to consider at least single and double promotions of the valence electrons to excited orbitals. In the case of the open $3d$ subshell, inclusion of all important promotions leads to extremely large configuration expansions and makes it very difficult to obtain accurate wave functions through standard multiconfiguration Hartree-Fock (MCHF) or configuration-interaction methods.

In the present work, we used the MCHF code of Froese-Fischer *et al.* [16] in combination with our CI code with nonorthogonal orbitals to generate the target wave functions. These calculations closely follow the structure calculations in our recent papers on BSR calculations for electron collisions with Fe I [14] and Fe II [15]. Since our method is the same as that described in the above papers, we refer to the latter for the computational details. Here we will concentrate only on the specific aspects of the present calculations.

Our approach for the modeling of atomic wave functions has two characteristic features, that distinguish it substantially from nearly all other methods commonly used to describe electron-atom collisions or photoionization processes. The first important aspect of the BSR approach is the possibility of using term-dependent one-electron orbitals in the multiconfiguration description of the N-electron target states. In traditional methods with an orthogonal set of one-electron orbitals, a similar accuracy, in principle, can be achieved by very large expansions using additional correlated pseudo-orbitals. The term dependence of the valence orbitals, both in Fe I and Fe II, was found to be noticeable but not extremely strong, with a maximum change of the mean radius for the $3d$ electron up to 10%. However, the corresponding corrections in the configuration energies are around 0.2 Ry (2.7 eV). This makes accounting for the term dependence very important for accurate calculations of the term energies.

As another distinctive aspect of the present approach, we tried to account for all major correlation effects. The final configuration expansions contained the most important one- and two-electron excitations from the valence $3d$, $4s$, and $4p$ orbitals of the principal configurations. Inclusion of all possible promotions for the given case of the open $3d$ subshell leads to very large configuration expansions, with thousands of individual atomic configuration states that differ in the intermediate terms. Such target expansions cannot be used in the subsequent scattering calculations. Consequently, all previous calculations included only as many configurations as possible with the available computational resources, without analyzing the convergence of the target expansions. In the

TABLE I. Excitation energies (in eV) of the Fe I target levels included in the present photoionization calculations.

Index	Configuration	Term	Present	NIST [17]	Diff.	Index	Configuration	Term	Present	NIST [17]	Diff.
1	$3d^6 4s^2$	$a\,^5D$	0.00000	0.00000	0.000	23	$3d^7(^2H)4s$	$a\,^1H$	3.52020	3.52326	−0.003
2	$3d^7(^4F)4s$	$a\,^5F$	0.86082	0.87493	−0.014	24	$3d^6 4s^2$	$a\,^1I$	3.48480	3.58439	−0.003
3	$3d^7(^4F)4s$	$a\,^3F$	1.48145	1.48836	−0.007	25	$3d^6(^5D)4s4p$	$z\,^5P^o$	3.54575	3.58639	0.005
4	$3d^7(^4P)4s$	$a\,^5P$	2.16087	2.14265	0.018	26	$3d^6 4s^2$	$b\,^3D$	3.56252	3.58977	−0.003
5	$3d^6 4s^2$	$a\,^3P$	2.28122	2.30004	−0.019	27	$3d^6 4s^2$	$b\,^1G$	3.60328	3.64464	−0.004
6	$3d^6 4s^2$	$a\,^3H$	2.36601	2.37711	−0.011	28	$3d^6(^5D)4s4p$	$z\,^3D^o$	3.77607	3.86382	−0.003
7	$3d^6(^5D)4s4p$	$z\,^7D^o$	2.40412	2.38311	0.021	29	$3d^6(^5D)4s4p$	$z\,^3F^o$	3.82394	3.87662	0.030
8	$3d^6 4s^2$	$b\,^3F$	2.54367	2.53060	0.013	30	$3d^8$	$c\,^3F$	4.05592	4.07445	0.015
9	$3d^6 4s^2$	$a\,^3G$	2.67804	2.67132	0.007	31	$3d^7(^4F)4p$	$y\,^5D^o$	4.13847	4.10398	−0.006
10	$3d^7(^4P)4s$	$b\,^3P$	2.77262	2.78906	−0.016	32	$3d^7(^4F)4p$	$y\,^5F^o$	4.16598	4.18009	−0.018
11	$3d^6(^5D)4s4p$	$z\,^7F^o$	2.77755	2.79275	−0.015	33	$3d^6(^5D)4s4p$	$z\,^3P^o$	4.16824	4.18450	−0.064
12	$3d^6 4s^2$	$a\,^1S$	2.80530			34	$3d^7(^2D)4s$	$b\,^1D$	4.23998	4.24445	0.005
13	$3d^7(^2G)4s$	$b\,^3G$	2.93034	2.93053	−0.000	35	$3d^7(^4F)4p$	$z\,^5G^o$	4.32527	4.30728	−0.017
14	$3d^6(^5D)4s4p$	$z\,^7P^o$	2.93705	2.93277	0.004	36	$3d^7(^4F)4p$	$z\,^3G^o$	4.37188	4.37506	−0.019
15	$3d^7(^2P)4s$	$c\,^3P$	2.98683	2.99573	−0.009	37	$3d^7(^2F)4s$	$d\,^3F$	4.51238	4.53713	−0.000
16	$3d^7(^2G)4s$	$a\,^1G$	3.00166	2.99691	0.005	38	$3d^6(^5D)4s4p$	$y\,^5P^o$	4.57776	4.54064	−0.014
17	$3d^6(^5D)4s4p$	$z\,^5D^o$	3.17777	3.19232	−0.015	39	$3d^7(^4F)4p$	$y\,^3F^o$	4.49736	4.54289	−0.062
18	$3d^7(^2H4s$	$b\,^3H$	3.20414	3.21453	−0.010	40	$3d^7(^2F)4s$	^1F	4.53208		
19	$3d^7(^2D)4s$	$a\,^3D$	3.21687	3.22250	−0.006	41	$3d^7(^4F)4p$	$y\,^3D^o$	4.76043	4.72430	0.024
20	$3d^6(^5D)4s4p$	$z\,^5F^o$	3.30659	3.32482	−0.018	42	$3d^8$	^1D	4.73248		
21	$3d^7(^2P)4s$	$a\,^1P$	3.35960	3.36494	−0.005	43	$3d^6(^5D)4s4p$	$x\,^5D^o$	4.86200	4.90585	−0.006
22	$3d^6 4s^2$	$a\,^1D$	3.49993	3.49656	0.003	44	$3d^6(^5D)4s4p$	$x\,^5F^o$	4.97766	4.98932	−0.012

present approach, we attempted to include the most important correlation effects. To do that, we first analyzed the full target expansions, which contained all double promotions, to determine the correlation configurations that matter most. This analysis allowed us to choose the configurations that should be included in the final target expansions, while at the same time keeping these expansions to a manageable size that was still appropriate for the subsequent scattering calculations.

For the Fe I wave functions, the list of most important configurations is discussed in Ref. [14]. In the present calculations, we chose to keep all configurations with mixing coefficients of magnitude larger than ∼0.01. This cut-off parameter is smaller than in our treatment of electron scattering from Fe I. The resulting CI expansions with sizes between 400 and 1200 for each LS target state are still suitable for photoionization calculations on modern state-of-the-art computational facilities. We also applied a semiempirical correction using the cut-off parameter to adjust the theoretical LS energies to the experimental values obtained by taking a weighted average over the fine-structure levels [17]. Due to different convergence rates for the individual terms, this required us to vary the cut-off parameters in the magnitude range between 0.008 and 0.015 for the various terms. The fastest convergence was achieved for states with high multiplicity, ^7L and ^5L terms, whereas the singlet and triplet states exhibit a very slow convergence pattern.

Table I compares the calculated LS excitation energies with the experimental values for all Fe I states included in the present photoionization calculations. The experimental excitation energies were taken from the NIST compilation [17] where possible. For some of the higher-lying levels, however, no observed values are available. As seen from the table,

the above procedure allowed us to obtain agreement with the observed LS energies to better than 0.1 eV for all states included. The agreement with the experimental energy levels is considerably better than in any other previous scattering calculation for collisions with Fe II that we are aware of. Using the larger configuration expansions also improved the agreement in comparison to our previous calculation [14]. One important consequence is the shift of the $3d^6 4s^2\ ^1S$ state to higher energies. The exact position of this state is still an open question and calls for additional experimental data.

The target representation of the Fe II states was constructed following the one used in our recent work on electron-impact excitation of singly ionized iron [15]. We included all LS terms of the $3d^6 4s$, $3d^5 4s^2$, $3d^7$, $3d^6 4p$, and $3d^5 4s4p$ configurations, with 261 terms overall. Table II lists the lowest predicted 98 LS terms of Fe II and compares the calculated energies with the experimental values. The full list of levels included in the present scattering calculations is given in the Supplemental Material [18]. Again, in constructing the target wave functions, we first checked all double promotions for the principal configurations and kept in the final expansions only the configurations with coefficients of magnitude larger than ∼0.025. The convergence of the target expansions for Fe II is faster than for neutral iron. The cut-off parameters for Fe II were chosen to (i) ensure consistency between the Fe I and Fe II expansions and (ii) to obtain the best possible agreement with the experimental photoionization thresholds. As seen from Table II, the agreement with the observed LS energies is better than 0.1 eV for most states, except for some doublet terms, for which the convergence was found to be going extremely slowly.

TABLE II. Excitation energies (in eV) of the Fe II final target levels included in the present photoionization calculations.

Index	Configuration	Term	Present	NIST [17]	Diff.	Index	Configuration	Term	Present	NIST [17]	Diff.
1	$3d^6(^5D)4s$	$a\,^6D$	0.00000	0.00000	0.000	51	$3d^6(^3P)4p$	$y\,^4D^o$	7.68767	7.67642	0.012
2	$3d^7$	$a\,^4F$	0.22873	0.23746	−0.008	52	$3d^6(^3H)4p$	$z\,^2I^o$	7.75384	7.68254	0.071
3	$3d^6(^5D)4s$	$a\,^4D$	1.00085	0.98236	0.019	53	$3d^6(^3F)4p$	$x\,^4D^o$	7.79919	7.78729	0.012
4	$3d^7$	$a\,^4P$	1.61611	1.64122	−0.025	54	$3d^6(^3F)4p$	$z\,^2F^o$	7.93216	7.92629	0.006
5	$3d^7$	$a\,^2G$	1.97335	1.93060	0.042	55	$3d^6(^3F)4p$	$y\,^4G^o$	7.96447	7.87869	0.086
6	$3d^7$	$a\,^2P$	2.15249	2.25549	−0.102	56	$3d^6(^3P)4p$	$z\,^2P^o$	7.98689	7.98813	−0.001
7	$3d^7$	$a\,^2H$	2.45967	2.48451	−0.025	57	$3d^6(^3F)4p$	$y\,^2G^o$	8.02078	7.99718	0.024
8	$3d^7$	$a\,^2D$	2.52821	2.52757	0.000	58	$3d^6(^3H)4p$	$z\,^2H^o$	8.05252	8.05993	−0.007
9	$3d^6(^3H)4s$	$a\,^4H$	2.59340	2.60163	−0.009	59	$3d^6(^3G)4p$	$x\,^4G^o$	8.14564	8.09909	0.047
10	$3d^6(^3P)4s$	$b\,^4P$	2.62235	2.61313	0.009	60	$3d^54s^2$	^2I	8.16405		
11	$3d^6(^3F)4s$	$b\,^4F$	2.78328	2.77477	0.008	61	$3d^6(^3G)4p$	$x\,^4F^o$	8.16627	8.16450	0.002
12	$3d^54s^2$	$a\,^6S$	2.94341	2.84212	0.101	62	$3d^6(^3P)4p$	$z\,^2S^o$	8.18361	8.16489	0.019
13	$3d^6(^3G)4s$	$a\,^4G$	3.12934	3.13143	−0.002	63	$3d^6(^3G)4p$	$y\,^4H^o$	8.19170	8.19302	−0.001
14	$3d^6(^3P)4s$	$b\,^2P$	3.13657	3.20920	−0.072	64	$3d^6(^3F)4p$	$y\,^2D^o$	8.27347	8.26940	0.005
15	$3d^6(^3H)4s$	$b\,^2H$	3.16495	3.20032	−0.035	65	$3d^6(^3G)4p$	$y\,^2H^o$	8.35303	8.33407	0.019
16	$3d^6(^3F)4s$	$a\,^2F$	3.33076	3.34805	−0.017	66	$3d^5(^6S)4s4p$	$x\,^4P^o$	8.53341	8.53496	−0.001
17	$3d^6(^3G)4s$	$b\,^2G$	3.77259	3.72956	0.043	67	$3d^6(^3G)4p$	$y\,^2F^o$	8.58723	8.58270	0.004
18	$3d^6(^3D)4s$	$b\,^4D$	3.84077	3.84398	−0.003	68	$3d^6(^3G)4p$	$x\,^2G^o$	8.70428	8.67498	0.029
19	$3d^7$	$b\,^2F$	3.88267	3.90300	−0.020	69	$3d^6(^1I)4p$	$z\,^2K^o$	8.76101	8.76208	−0.001
20	$3d^6(^1I)4s$	$a\,^2I$	3.97082	4.02791	−0.057	70	$3d^6(^3D)4p$	$w\,^4P^o$	8.84826	8.88371	−0.036
21	$3d^6(^1G)4s$	$c\,^2G$	4.08447	4.10141	−0.016	71	$3d^6(^1G)4p$	$x\,^2H^o$	8.85140	8.89788	−0.047
22	$3d^6(^1D)4s$	$b\,^2D$	4.43813	4.43693	0.001	72	$3d^6(^3D)4p$	$w\,^4F^o$	8.90035	8.91993	−0.020
23	$3d^6(^1S)4s$	$a\,^2S$	4.58154	4.56669	0.015	73	$3d^54s^2$	^2D	8.92103		
24	$3d^6(^1D)4s$	$c\,^2D$	4.69523	4.68494	0.010	74	$3d^6(^3D)4p$	$y\,^2P^o$	8.97058	9.02530	−0.054
25	$3d^6(^5D)4p$	$z\,^6D^o$	4.75973	4.74993	0.010	75	$3d^6(^3D)4p$	$w\,^4D^o$	8.99030	8.94838	0.042
26	$3d^6(^5D)4p$	$z\,^6F^o$	5.16594	5.17773	−0.012	76	$3d^6(^1G)4p$	$x\,^2F^o$	9.01599	9.00526	0.011
27	$3d^6(^5D)4p$	$z\,^6P^o$	5.20962	5.28105	−0.071	77	$3d^54s^2$	^4F	9.03412	9.05750	−0.024
28	$3d^6(^5D)4p$	$z\,^4D^o$	5.50673	5.49889	0.008	78	$3d^6(^1G)4p$	$w\,^2G^o$	9.06308	9.01479	0.048
29	$3d^6(^5D)4p$	$z\,^4F^o$	5.53536	5.48273	0.052	79	$3d^6(^1I)4p$	$w\,^2H^o$	9.17151	9.08044	0.092
30	$3d^6(^1F)4s$	$c\,^2F$	5.55258	5.52035	0.033	80	$3d^6(^1I)4p$	$y\,^2I^o$	9.17182	9.12188	0.050
31	$3d^6(^5D)4p$	$z\,^4P^o$	5.81800	5.80783	0.010	81	$3d^6(^3D)4p$	$x\,^2D^o$	9.27329	9.19346	0.080
32	$3d^7$	$d\,^2D$	5.88559	5.88137	0.005	82	$3d^6(^3D)4p$	$w\,^2F^o$	9.37622	9.33504	0.041
33	$3d^6(^3P)4s$	$c\,^4P$	6.12668	6.10941	0.018	83	$3d^54s^2$	^2H	9.46116		
34	$3d^6(^3F)4s$	$c\,^4F$	6.14797	6.16717	−0.019	84	$3d^6(^1S)4p$	$x\,^2P^o$	9.50251	9.41375	0.089
35	$3d^5(^6S)4s4p$	$z\,^8P^o$	6.41902	6.46488	−0.046	85	$3d^6(^1D)4p$	$w\,^2D^o$	9.64397	9.69309	−0.049
36	$3d^54s^2$	$b\,^4G$	6.63719	6.67744	−0.040	86	$3d^54s^2$	^2G	9.66463	9.65807	0.007
37	$3d^6(^3P)4s$	$c\,^2P$	6.68545	6.71651	−0.031	87	$3d^6(^1D)4p$	$v\,^2F^o$	9.74585	9.60628	0.140
38	$3d^6(^3F)4s$	$d\,^2F$	6.78306	6.75557	0.027	88	$3d^6(^1D)4p$	$w\,^2P^o$	9.74831	9.75612	−0.008
39	$3d^54s^2$	$d\,^4P$	7.09130	7.07691	0.014	89	$3d^5(^6S)4s4p$	$x\,^6P^o$	9.82455	9.78097	0.044
40	$3d^6(^1G)4s$	$d\,^2G$	7.23205	7.22148	0.011	90	$3d^6(^1D)4s$	^2D	9.86203		
41	$3d^54s^2$	$c\,^4D$	7.45346	7.43373	0.020	91	$3d^54s^2$	^2F	10.09509	10.07702	0.018
42	$3d^6(^3P)4p$	$y\,^4P^o$	7.47165	7.48849	−0.016	92	$3d^5(^4P)4s4p$	$^6S^o$	10.20182		
43	$3d^6(^3P)4p$	$z\,^2D^o$	7.50941	7.56838	−0.059	93	$3d^54s^2$	^2D	10.23813		
44	$3d^6(^3H)4p$	$z\,^4G^o$	7.51363	7.48416	0.030	94	$3d^5(^4G)4s4p$	$^6H^o$	10.25531		
45	$3d^6(^3H)4p$	$z\,^4H^o$	7.52415	7.50242	0.022	95	$3d^6(^1F)4p$	$v\,^2G^o$	10.28818	10.29877	−0.011
46	$3d^6(^3H)4p$	$z\,^4I^o$	7.54401	7.56593	−0.022	96	$3d^5(^4G)4s4p$	$^6G^o$	10.31784		
47	$3d^6(^3P)4p$	$z\,^4S^o$	7.60257	7.34842	0.255	97	$3d^6(^1F)4p$	$v\,^2D^o$	10.36428	10.36977	−0.006
48	$3d^5(^6S)4s4p$	$y\,^6P^o$	7.61886	7.64508	−0.026	98	$3d^6(^1F)4p$	$u\,^2F^o$	10.70068	10.67576	0.025
49	$3d^6(^3F)4p$	$y\,^4F^o$	7.62258	7.65407	−0.031	...					
50	$3d^6(^3H)4p$	$z\,^2G^o$	7.65804	7.65527	0.003	261	$3d^5(^2D)4s4p$	$^2P^o$	24.10451		

B. Photoionization calculations

For the photoionization calculations we employed a parallelized version of the BSR code [13], which is based on the R-matrix method to solve the close-coupling equations. The distinctive feature of the code is the use of B splines as a universal basis to represent the scattering orbitals in the inner region, $r \leqslant a$. Hence, the R-matrix expansion in this region takes the form

$$\Psi_k(x_1, \ldots, x_{N+1})$$
$$= \mathcal{A} \sum_{ij} \bar{\Phi}_i(x_1, \ldots, x_N; \hat{\mathbf{r}}_{N+1}\sigma_{N+1}) r_{N+1}^{-1} B_j(r_{N+1}) a_{ijk}$$
$$+ \sum_i \chi_i(x_1, \ldots, x_{N+1}) b_{ik}. \quad (1)$$

Here $\mathcal{A}$ denotes the antisymmetrization operator, $\bar{\Phi}_i$ are the channel functions, and the splines $B_j(r)$ represent the continuum orbitals. The principal advantage of B splines is that they form an effectively complete basis, and hence no Buttle correction to the R matrix is needed in this case. The amplitudes of the wave functions at the boundary, which are required for the evaluation of the R matrix, are given by the coefficient of the last spline, which is the only spline with nonzero value at the boundary.

The other important feature of the present code concerns the orthogonality requirements for the one-electron radial functions. We impose only limited orthogonal conditions between the bound and continuum orbitals. Specifically, for the present calculations, we only require the orthogonality of the continuum orbitals to the bound orbitals in the filled $1s$, $2s$, $2p$, $3s$, and $3p$ subshells. No orthogonality constraints were imposed to the spectroscopic excited orbitals or the correlated orbitals. As a result, the $(N + 1)$-electron configurations χ_i in the second part of Eq. (1) can be completely avoided. This facilitates keeping the scattering and bound parts of the close-coupling expansions consistent with each other and avoids the pseudo-resonance structure that sometimes appears in standard R-matrix calculations due to an inconsistency between the scattering and bound parts of the close-coupling expansions.

The close-coupling expansion in our calculations included the 261 states of singly ionized iron listed in Table II. While some of these states, mainly with configuration $3d^5 4s 4p$, are located above the ionization threshold, they may have a large influence due to the strong $3d - 4p$ and $4s - 4p$ dipole transition. This model is referred to as BSR-261 below. The partial-wave CC expansions in this model contained up to 359 different scattering channels in the LS-coupling scheme when restricting the scattering functions to include only ks, kp, kd, and kf continuum orbitals. In the internal region with radius $a = 25 a_0$ (where $a_0 = 0.529 \times 10^{-10}$ m is the Bohr radius), the continuum orbitals were represented by 78 B splines of order 8. The most complex features of the present e-Fe II calculation are the large configuration expansions for the total scattering functions ($\sim 100\,000$ terms) and the extremely large number of two-electron matrix elements. This is partly due to the open $3d$ subshell configurations, but the principal complication originates in the huge number of overlap factors due to the nonorthogonal orbitals. In order to deal with this situation,

a further optimization of the code for the determination of the angular coefficients and the subsequent construction of the Hamiltonian matrix were required.

In R-matrix theory, the photoionization cross section is defined through the dipole matrix elements between the initial state Ψ_0 and the R-matrix basis states Ψ_k, provided that all radial orbitals of the initial state are well confined to the inner region. The total photoionization cross section (in a_0^2) for a photon energy ω (in Rydberg) and an initial state with total orbital angular momentum L_0 is given by

$$\sigma(\omega) = \frac{8}{3}\pi^2 \alpha \, \omega^{\pm 1} \, \frac{1}{(2L_0 + 1)} \sum_j |(\Psi_j^- \|D\| \Psi_0)|^2, \quad (2)$$

where $\alpha \approx 1/137$ is the fine-structure constant and D is the electric dipole operator. The powers of ω (+1 or −1) correspond to the length and velocity forms, respectively. The index j runs over the various open channels. The solutions Ψ_j^- correspond to asymptotic conditions with a plane wave in the direction of the ejected electron momentum $\mathbf{k}$ and ingoing waves in all open channels.

Expanding the Ψ_j^- in terms of the R-matrix states, we find

$$(\Psi_j^- \|D\| \Psi_0) = \frac{1}{a} \sum_k \frac{(\Psi_k \|D\| \Psi_0)}{E_k - E_0 - \omega} \, \mathbf{w}_k^T \mathbf{R}^{-1} \mathbf{F}_j^-(a), \quad (3)$$

where $(\Psi_k \|D\| \Psi_0)$ are reduced matrix elements between the initial state and the R-matrix basis functions, $\mathbf{w}_k^T$ stands for the surface amplitudes of the inner-region solutions at $r = a$, and $\mathbf{R}^{-1}$ is the inverse of the R matrix [13]. The energies E_k and E_0 are also in Rydberg. $F_i(r)$ stands for the radial wave function of the scattered electron. The program ASYPCK [19], which can directly use the BSR inner-region results as input, was used to generate the asymptotic solutions $\mathbf{F}$.

III. RESULTS AND DISCUSSION

We begin our discussion with photoionization of some low-lying metastable states of Fe I. Figure 1 presents the predicted photoionization cross sections as a function of photon energy for a sample of even-parity states. These examples include both the $3d^6 4s^2$ and $3d^7 4s$ configurations with quintet, triplet, and singlet terms. The figure also presents a thorough comparison with the most recent 134-state R-matrix calculations of Bautista *et al.* [3]. This model is referred to as RM-134 or RM below. Earlier calculations mentioned in the Introduction were discussed in Refs. [3,10], where large differences with the extended R-matrix results were found. The early calculations are not considered reliable and hence will not be discussed any further.

All panels in Fig. 1 show a complex resonance structure. In order to delineate in detail the autoionization resonances near the ionization thresholds, we used a fine energy step of 10^{-4} Ry in the range of up to 2.0 Ry for the ejected electron. This covers all states of the residual Fe II ions considered here. As seen from the figure, the resonance structure consists of a few wide and strong resonances at low photon energies and numerous narrow but extensive resonances over a wide range of energies. The background cross sections for all transitions are very similar, both in shape and magnitude. As will be shown below, they are mainly defined by direct ionization of
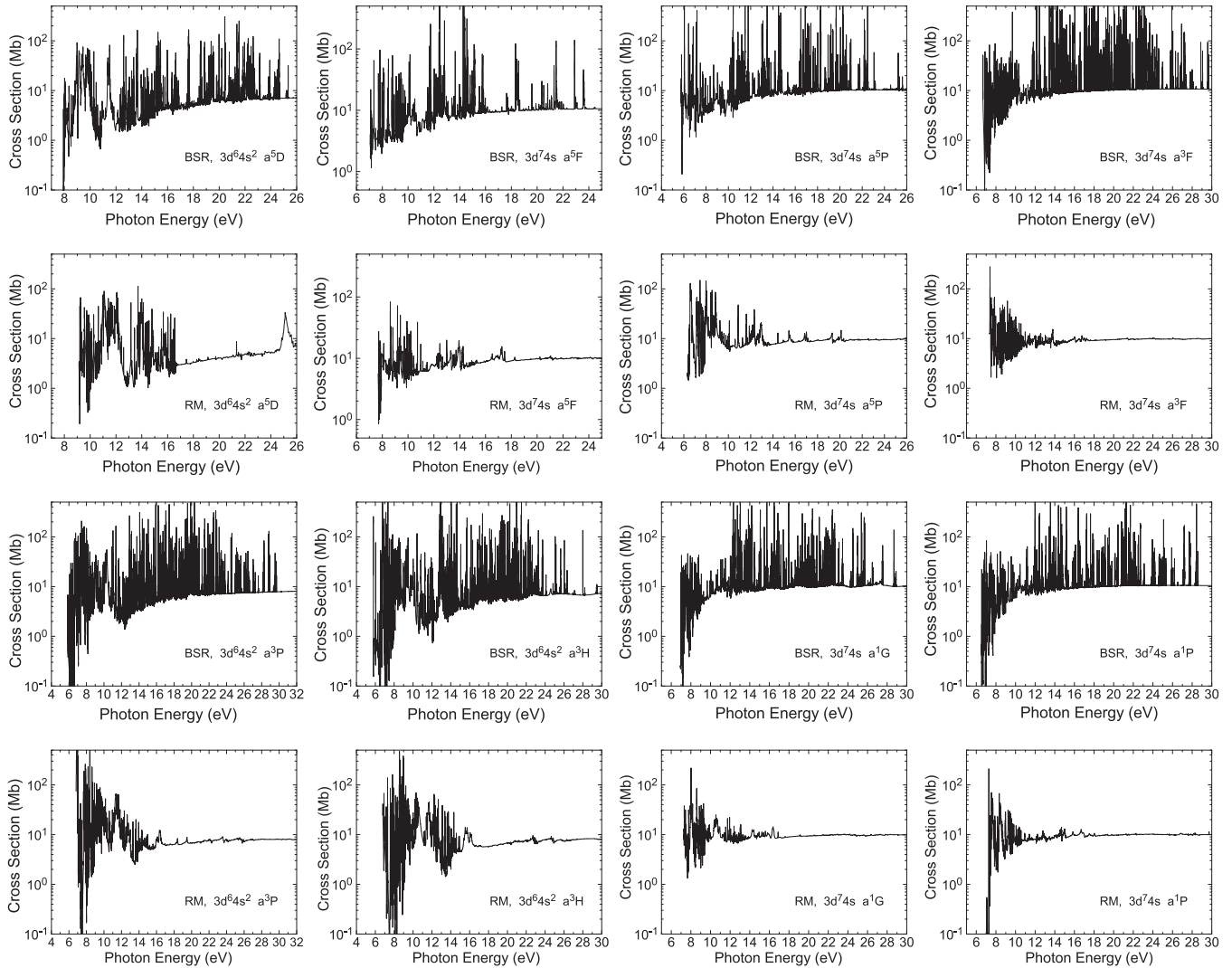
FIG. 1. Photoionization cross sections as a function of photon energy for a sample of low-lying even-parity states of Fe I. The present BSR-261 (BSR in the legend, first and third row) predictions are compared with the RM-134 (RM in the legend, second and fourth row) results of Bautista *et al.* [3].

the $3d$ electron, and hence all of them have approximately the same value of about 10 Mb at higher energies.

While there is close agreement between the present BSR-261 calculations and the RM-137 results [3] regarding the background cross sections, the present cross sections exhibit a much more extensive resonance structure, especially at higher energies. This is directly connected to the more extensive close-coupling expansions in our calculation. For example, the photoionization cross section for the ground state, $3d^6 4s^2 \ ^5D$, exhibits two strong and wide resonance peaks at low energies and a set of narrow resonances at higher energies. They cover the entire region up to the highest ionization threshold, $3d^5(^2D)4s4p \ 2P^o$, included in the present expansion. Qualitatively, the same structure is also found in the RM-137 calculations, approximately with the same height of the resonance peaks but over a smaller range of energies. The differences in the positions of the resonances are related to the different position of the ionization thresholds. As discussed above, the present ionization thresholds agree with the experimental values to generally better than 0.1 eV.

As seen from Fig. 1, the most extensive resonance structure was found for photoionization of the triplet states. Examples are given for the $3d^7 4s \ ^3F$ and $3d^5 4s^2 \ ^3P$ and ^3P states. In the LS approximation, photoionization of the triplet states leads to the largest close-coupling expansions and, consequently, to the most complex resonance structure. The largest difference between the BSR and RM predictions was found for photoionization of the singlet states. This suggests that the RM-134 model missed many important final states of the residual ion. Overall, the comparison the BSR-261 and RM-134 models shows that inclusion of the entire set of terms for the final states has a significant influence on the details of the resonance structure.

In practical applications, particularly for nonlocal thermodynamic equilibrium modeling, it is important to accurately determine the population in the excited levels of the residual ion following photoionization. In this respect, the cross sections for partial processes from both the ground and the low-lying excited states are required. Our calculations revealed that photoionization of Fe I leads to population of
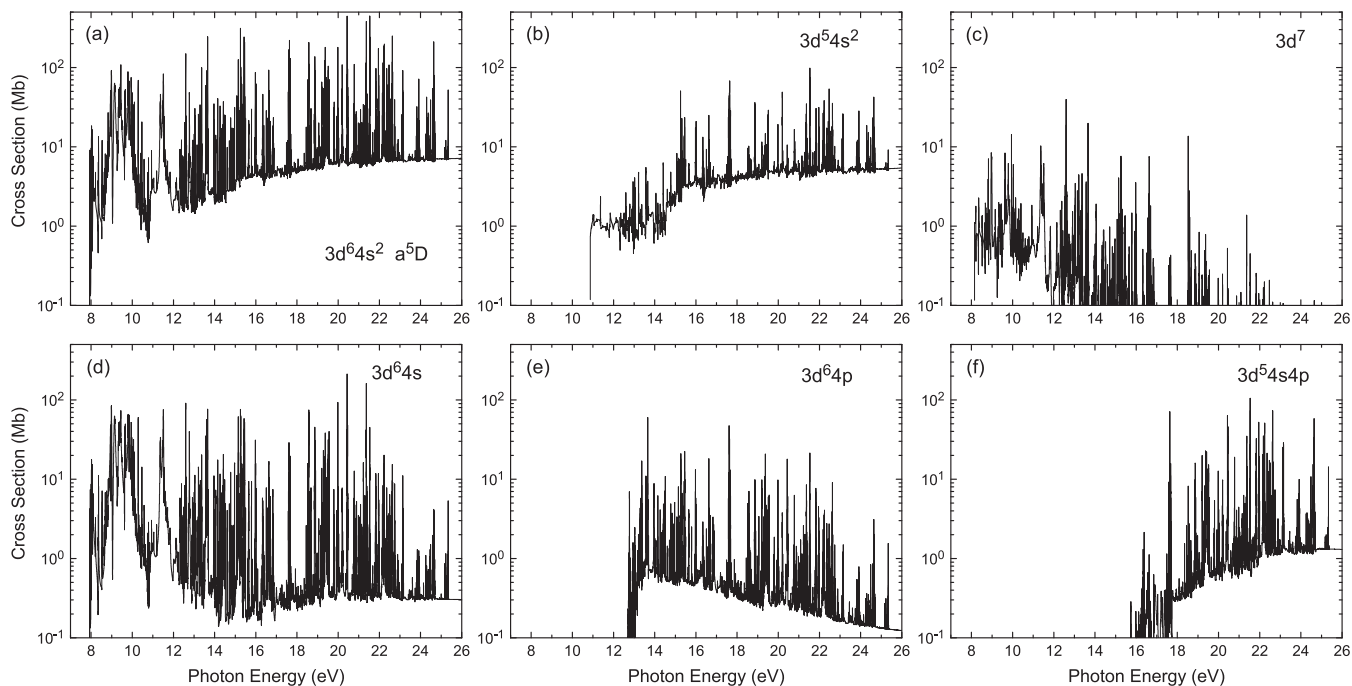
FIG. 2. Photoionization cross section of the $3d^64s^2\,^5D$ ground state of Fe I (a), along with the contributions from different subsets (b)–(f) of final ionic configurations indicated in the legend.

many levels of Fe II, generally with no dominant channel in the photoionization of the given initial state. This is due to the complex spectra of Fe II, where the ionic configurations with an open $3d$ subshell contain many states with different total and intermediate terms. To illustrate this point, Figs. 2 and 3 present partial cross sections for the lowest-lying states of two important configurations, $5d^64s^2\,^5D$ and $5d^74s\,^5P$,

respectively. Due to numerous possible final states, the figures present the summed cross sections from various subsets of levels of Fe II belonging to a given configuration. Our electronically available tables, however, contain partial cross sections for all individual states of Fe II.

For photoionization of the ground state $3d^64s^2\,^5D$, presented in Fig. 2, the dominant channel at low energies is
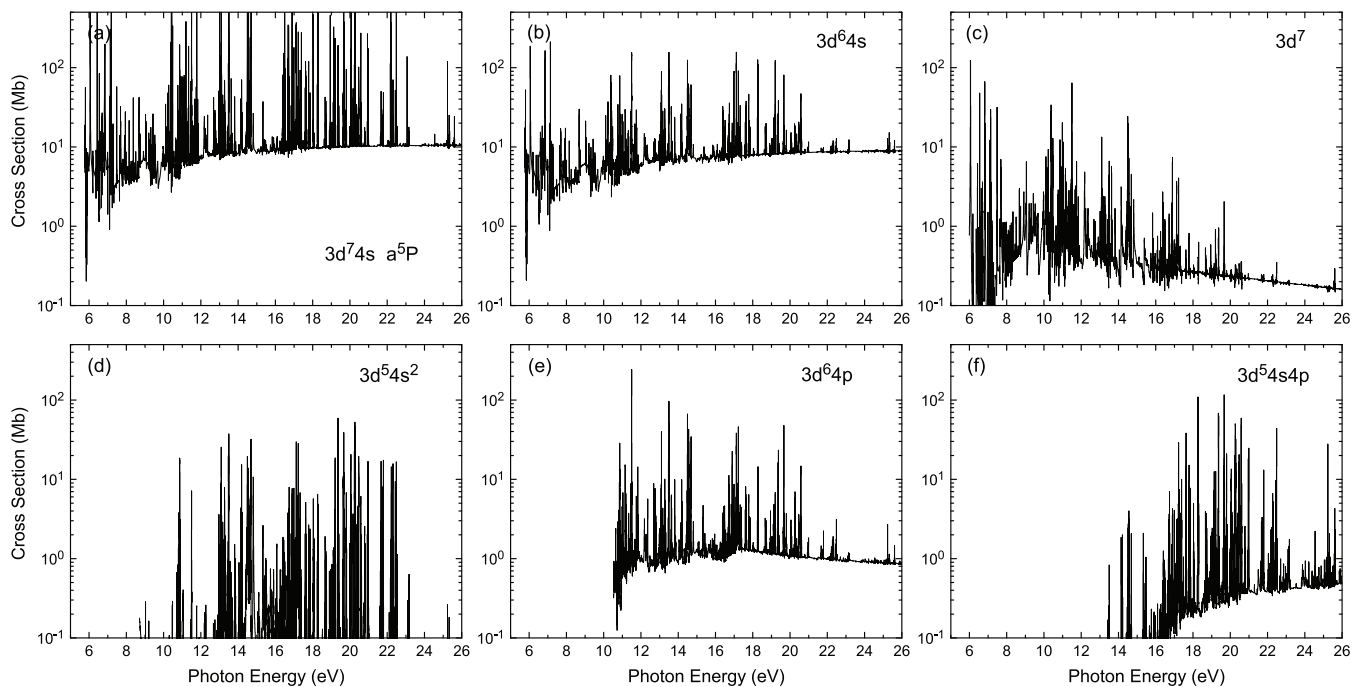
FIG. 3. Photoionization cross section of the $3d^74s\,^5P$ excited state of Fe I (a), along with the contributions from different subsets (b)–(f) of final ionic configurations indicated in the legend.
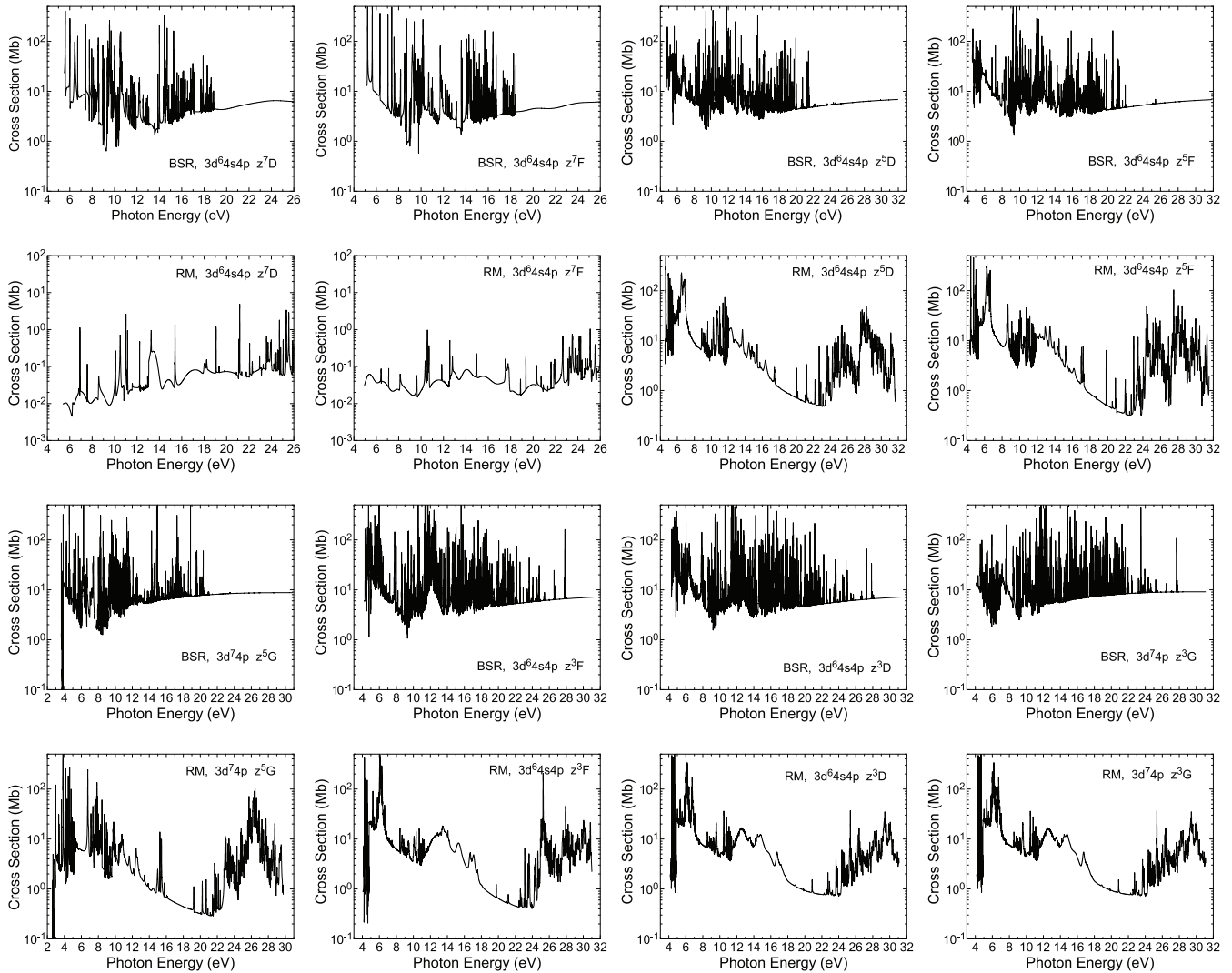
FIG. 4. Photoionization cross section for transitions from the first few odd-parity excited terms of Fe I. The present BSR-261 (BSR in the legend, first and third row) predictions are compared with the RM-134 (RM in the legend, second and fourth row) results of Bautista *et al.* [3].

4*s* ionization, leading to final ionic states with configuration $3d^6 4s$. As shown in a more detailed comparison, the cross section is dominated by ionization to the ground state $3d^6 4s\, ^6D$ of Fe II. These channels also exhibit the most extensive resonance structure. Above 11 eV, channels with $3d$ ionization open up and ionization to final ionic states with configuration $3d^5 4s^2$ becomes dominant. These channels define the magnitude of the total photoionization cross sections at higher energies. As illustrated in the other panels, ionization with additional excitation to the $3d^6 4p$ and $3d^5 4s4p$ target states is also noticeable. This process is expected to be important due to the strong $4s - 4p$ and $3d - 4p$ transitions. These cross sections exhibit a different energy dependence of the background. Ionization of $4s$ with excitation to the $3d^6 4p$ target states shows a near-threshold maximum with subsequent decrease in value, whereas $3d$ ionization with excitation to the $3d^5 4s4p$ target states shows increasing cross sections over a wide range of energies. We also see a considerable population of the $3d^7$ states, something that is not possible in a one-electron approximation. Such transitions occur due

to channel coupling and the decay of resonances into these states.

A similar picture for the partial cross sections is also observed for photoionization of the $3d^7 4s\, ^5P$ state shown in Fig. 3. Ionization of the $4s$ electron here leads to the $3d^7$ final ionic states. However, $3d$ ionization, with the $3d^6 4s$ final ionic states, dominates in this case for all energies. Ionization with excitation is also an important factor here and leads to noticeable population of the $3d^6 4p$ and $3d^5 4s4p$ target states. Direct (one-electron) photoionization to the $3d^5 4s^2$ states is forbidden but occurs due to close-coupling effects. These cross sections show a very small background. We emphasize again that the above comparison shows summed partial cross sections. These include numerous individual final states but generally have no dominant ionization channel.

We now turn to the discussion of the photoionization of the odd-parity $3d^6 4p$ and $3d^5 4s4p$ states of Fe I. The comparison of the present BSR cross sections with the *R*-matrix calculations of Bautista *et al.* [3] is given in Fig. 4. The examples include terms with different multiplicities, from
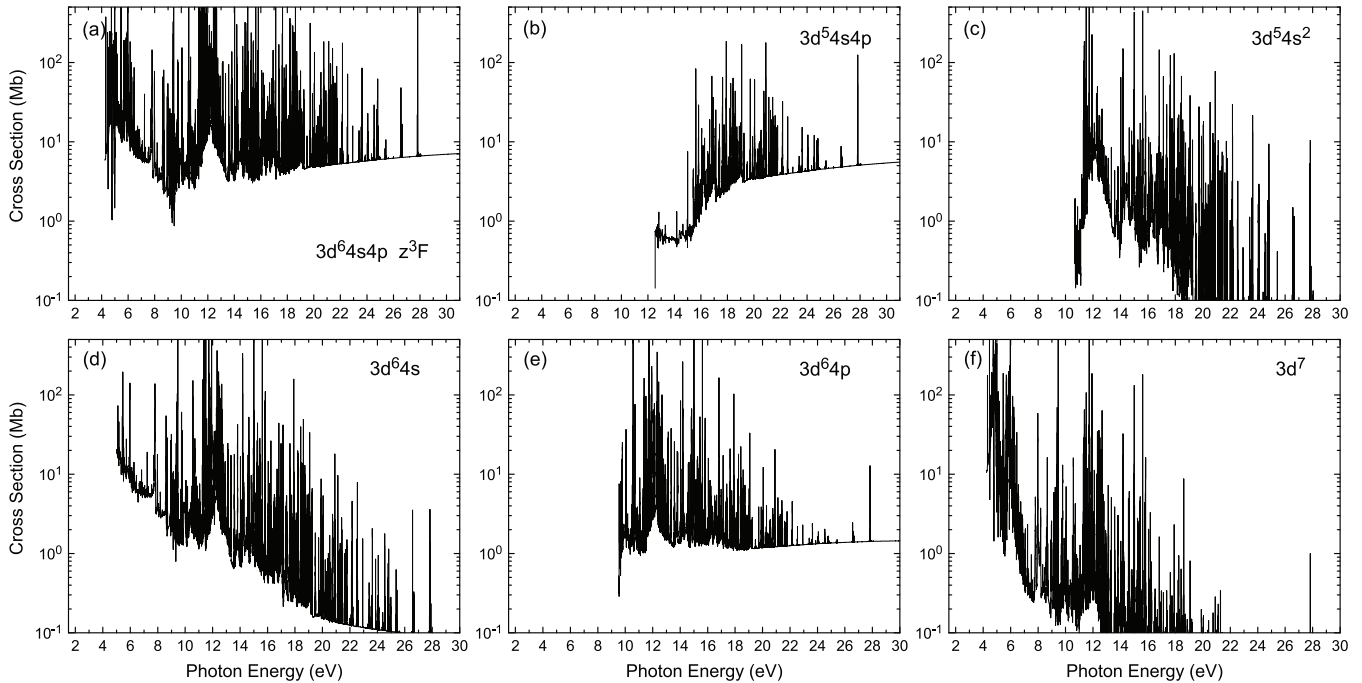
FIG. 5. Photoionization cross section of the $3d^6 4s4p$ z^3F state of Fe I (a), along with the contributions from different subsets (b)–(f) of final ionic configurations indicated in the legend.

$2S + 1 = 3 - 7$. In all cases we see many differences in the predicted cross sections, both regarding the energy dependence and the magnitude. The largest difference was found for ionization of the septet states, $3d^6 4s4p$ ^7D and ^7F. The RM-137 cross sections are much smaller (up to two orders of magnitude) than the present results for all energies and also reveal a different resonance structure. The RM-137 cross sections for the septet states also differ considerably from the previous R-matrix calculations [10] in the 55-state approximation. We suggest that the differences here may be due to some numerical issues rather than modeling the problem. For photoionization of the quintet and triplet states, the agreement between the BSR-261 and RM-134 results is much closer. At low energies, they agree at least in the magnitude, while they exhibit different resonance structures that agree only qualitatively. At higher energies, the BSR and RM calculations show a different energy dependence for the background cross sections. Whereas the BSR cross sections approach a near-constant plateau, the RM cross sections quickly decrease with increasing energy. This indicates that the RM close-coupling expansions omitted some important scattering channels connected to the $3d^5 4s4p$ final ionic stats. Furthermore, the RM cross sections indicate considerable resonance contributions at high energies above 20 eV, which is above the highest ionization threshold in their close-coupling expansion. Most likely, this resonance structure is unphysical and due to $(N+1)$-electron bound configurations in their R-matrix expansion. Recall that our BSR expansions (1) do not contain any such bound channels and hence the photoionization cross sections behave smoothly at high energies.

A more detailed analysis of different scattering channels for the photoionization of the odd-parity states is given in Fig. 5 for the $3d^6 4s4p$ z^3F state and in Fig. 6 for the

$3d^7 4p$ z^3G state, to provide just two examples. The $3d^6 4s4p$ states have three main photoionization channels, related to ionization of the $3d$, $4s$, or $4p$ electrons. Ionization of the outer $4p$ electron leads mostly to the $3d^6 4s$ ionic states. As seen from the example for the $3d^6 4s4p$ z^3F state, the corresponding partial cross sections provide the main contribution in the near-threshold region but they quickly decrease with increasing energy. The ionization of the $4s$ electron, on the other hand, leads to the $3d^6 4p$ ionic states. The background cross sections for this partial wave change slowly with energy. Overall, the contribution from $4s$ ionization to the total cross section is ∼25%. The main contribution to the total cross sections at higher energies originates from $3d$ ionization, which leads to the $3d^6 4s4p$ final ionic states. Omitting some of these states in the RM-134 calculations is likely the principal reason for the differences at higher energies. The contribution of the $3d^7$ and $3d^6 4s^2$ channels is also considerable and results mainly in an additional resonance structure. The background cross sections are very small in this case and are due to close-coupling effects.

Partial cross sections for photoionization of the $3d^7 4p$ z^3G state are shown in Fig. 6 and exhibit a similar energy dependence. In this case, $4p$ ionizations leads to the $3d^7$ ionic states and contributes mainly in the near-threshold region. The main contribution at higher energies is again due to $3d$ ionization leading to the $3d^6 4p$ ionic states. We also see a considerable contribution of the $3d^6 4s$ channels, which is due to close-coupling effects and strong configuration mixing of the ionic states. The $3d^5 4s^2$ and $3d^5 4s4p$ ionic states are populated mainly through resonant excitation. Overall, we note that photoionization of neutral iron leads to numerous scattering channels, and the relative population of the ionic states changes considerably when varying the photon energy.
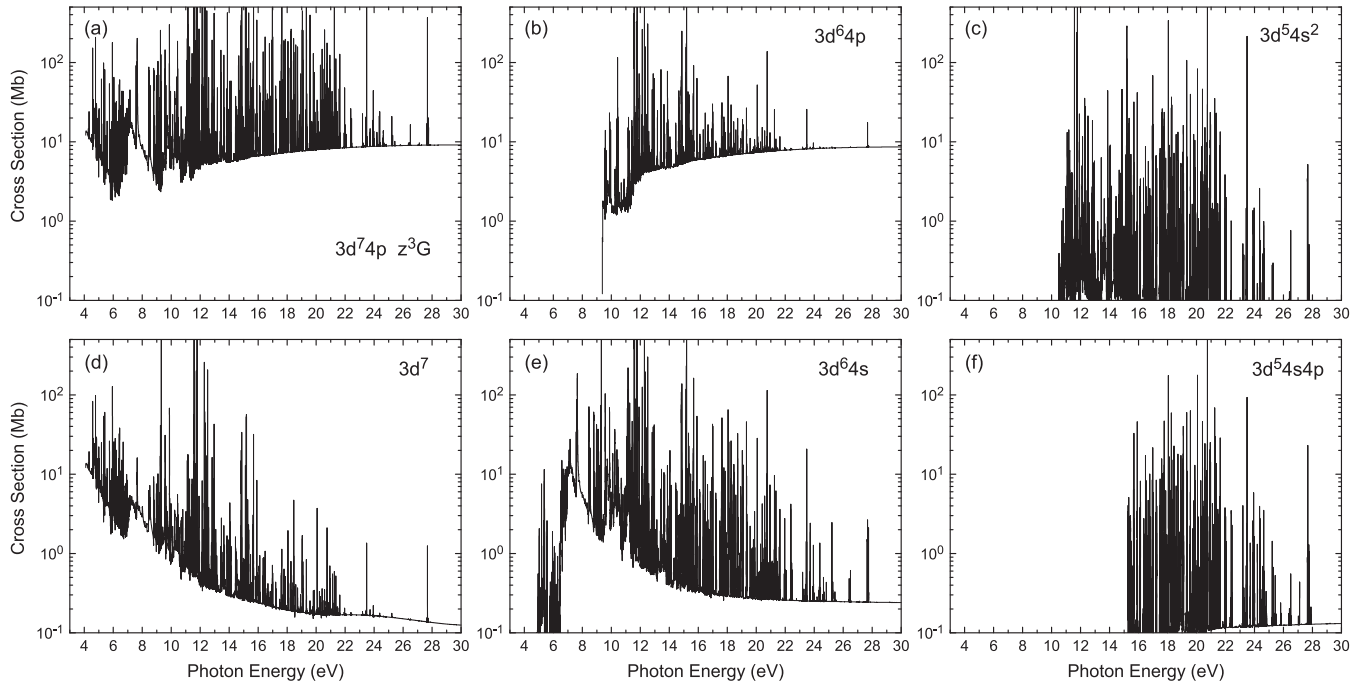
FIG. 6. Photoionization cross section of the $3d^74p\,z^3G$ state of Fe I (a), along with the contributions from different subsets (b)–(f) of final ionic configurations indicated in the legend.

IV. SUMMARY

We have presented predictions of photoionization cross sections for the ground and first excited states of Fe I. The chosen states cover all principal configurations and angular symmetries of neutral iron. The calculations were performed with the advanced BSR code [13], which employs the *R*-matrix method in a *B*-spline basis to solve the close-coupling equations. To represent the target states, we used extensive multiconfiguration expansions with carefully chosen configurations. We also employed term-dependent one-electron orbitals to accurately represent relaxation effects. This distinctive feature of the present calculations allowed us to generate a more accurate description of the Fe I and Fe II target states than those employed before.

The present calculations adopted a much larger close-coupling expansion than in previous works. Our expansion contains 261 *LS* states of Fe II and includes all levels of the $3d^64s$, $3d^54s^2$, $3d^7$, $3d^64p$, and $3d^54s4p$ configurations. The predicted photoionization cross sections exhibit significant differences with respect to earlier results, in particular with the most recent *R*-matrix calculations of Bautista *et al.* [3]. We argue that none of the previous calculations can be considered converged due to the omissions of important states in the residual-ion expansions. For example, photoionization of the $3d^64s4p$ states of Fe I can occur in the one-electron approximation through ionization of the $3d$, $4s$, or $4p$ electron, respectively, thus leading to the $3d^54s4p$, $3d^64p$, and $3d^64s$ final ionic states of Fe II. To obtain the convergence results, all these channels should be considered on equal footing. In particular, we found that $3d$ ionization becomes the dominant channel for higher energies. This leads to approximately the same value of the photoionization cross sections for all Fe I states.

We obtained total and partial photoionization cross sections for the first 44 bound states of Fe I. The photoionization of neutral iron exhibits numerous scattering channels. We performed a detailed analysis of the different channels, showing that the relative population of the different ionic states changed considerably when varying the photon energy. In addition, we carefully delineated the autoionizing resonance structures.

Both the BSR and RM photoionization cross sections discussed above were obtained in the *LS* approximation and hence provide data for transitions between *LS* terms. We are planning to extend the present calculations to the semirelativistic Breit-Pauli approach, which includes the spin-orbit term mixing and will produce more detailed data for the transitions between *LSJ* fine-structure levels. Such calculations, however, are much more extensive and time-consuming. Our preliminary results for photoionization of the *J* levels of the ground-state term suggest that the absolute magnitude of most fine-structure cross sections can be very accurately reproduced from the *LS* results by using the appropriate recoupling transformation. In general, Breit-Pauli calculations would only be needed for photoionization of the excited states with strong term mixing, but even for those it may well be sufficient to obtain the mixing coefficients from structure calculations and combine them with the recoupling procedure.

We also note that further extensive calculations for Fe photoionization are currently being carried out by the Belfast group [20]. In line with the above arguments, for an "intermediate-Z" target like Fe with a nuclear charge of $Z = 26$, the preliminary results from semirelativistic Breit-Pauli and full-relativistic Dirac approaches were found to be very similar. We would expect the remaining differences to be

mainly due to differences in the structure models than to the collision parts of the calculation.

The numerical data for the total and partial cross sections are available from the authors upon request. For the reasons given above, especially regarding the structure part, the present results are expected to be considerably more accurate than those obtained before. We hope that they will be used as benchmark data in applications as well as to asses the quality of other calculations. Comparison with these results can be used to assess the uncertainties in the existing data sets.

[1] K. Lind, A. M. Amarsi, M. Asplund, P. S. Barklem, M. Bautista, M. Bergemann, R. Collet, D. Kiselman, J. Leenaarts, and T. M. D. Pereira, MNRAS **468**, 4311 (2017).

[2] P. S. Barklem, Astron. Astrophys. Rev. **24**, 9 (2016).

[3] M. A. Bautista, K. Lind, and M. Bergemann, Astron. Astrophys. **606**, A127 (2017).

[4] H. P. Kelly and A. Ron, Phys. Rev. A **5**, 168 (1972).

[5] H. P. Kelly, Phys. Rev. A **6**, 1048 (1972).

[6] R. F. Reilman and S. T. Manson, Astrophys. J. Suppl. Ser. **40**, 815 (1979).

[7] D. A. Verner, D. G. Yakovlev, I. M. Band, and M. B. Trzhaskovskaya, At. Data Nucl. Data Tables **55**, 233 (1993).

[8] K. L. Baluja, A. Hibbert, and M. Mohan, J. Phys. B: At. Mol. Phys. **19**, 3613 (1986).

[9] M. J. Sawey and K. A. Berrington, J. Phys. B **25**, 1451 (1992).

[10] M. A. Bautista, Astron. Astrophys. Suppl. Ser. **122**, 167 (1997).

[11] K. A. Berrington, W. B. Eissner, and P. H. Norrington, Comput. Phys. Commun. **92**, 290 (1995).

[12] P. G. Burke, V. M. Burke, and K. M. Dunseath, J. Phys. B **27**, 5341 (1994).

[13] O. Zatsarinny, Comput. Phys. Commun. **174**, 273 (2006).

[14] K. Wang, O. Zatsarinny, and K. Bartschat, Astrophys. J. **867**, 63 (2018).

[15] S. S. Tayal and O. Zatsarinny, Phys. Rev. A **98**, 012706 (2018).

[16] C. Froese-Fischer, G. Tachiev, G. Gaigalas, and M. R. Godefroid, Comput. Phys. Commun. **176**, 559 (2007).

[17] A. Kramida, Yu. Ralchenko, J. Reader, and NIST ASD Team, NIST Atomic Spectra Database (ver. 5.6.1), [Online], http://physics.nist.gov/asd [2019, February 23], National Institute of Standards and Technology, Gaithersburg, MD (2018).

[18] See Supplemental Material at http://link.aps.org/supplemental/10.1103/PhysRevA.99.023430 for machine-readable tables of the Fe I and Fe II energies.

[19] M. A. Crees, Comput. Phys. Commun. **19**, 103 (1980).

[20] R. T. Smyth, C. A. Ramsbottom, and C. P. Ballance, Galaxies **6**, 87 (2018).